Title

Photocurrent-driven transient symmetry breaking in the Weyl semimetal TaAs

Journal

Nature Materials, 21(1)

ISSN

1476-1122

Authors

Sirica, N

Orth, PP

Scheurer, MS

et al.

Publication Date

2022

DOI

10.1038/s41563-021-01126-9

Photocurrent-driven transient symmetry breaking in the Weyl semimetal TaAs

N. Sirica,[1,*] P. P. Orth,[2,3] M. S. Scheurer,[4,5] Y.M. Dai,[1,6] M.-C. Lee,[1] P. Padmanabhan,[1] L.T. Mix,[1] S. W. Teitelbaum,[7,8] M. Trigo,[7,8] L.X. Zhao,[9] G.F. Chen,[9] B. Xu,[9] R. Yang,[9] B. Shen,[10] C. Hu,[10] C.-C. Lee,[11] H. Lin,[12] T.A. Cochran,[13] S.A. Trugman,[1] J.-X. Zhu,[1] M.Z. Hasan,[13,14] N. Ni,[10] X.G. Qiu,[9] A.J. Taylor,[1] D.A. Yarotski,[1] and R.P. Prasankumar[1,†]

[1] *Center for Integrated Nanotechnologies, Los Alamos National Laboratory, Los Alamos, NM 87545, USA*
[2] *Ames Laboratory, Ames, IA, 50011, USA*
[3] *Department of Physics and Astronomy, Iowa State University, Ames, IA, 50011, USA*
[4] *Department of Physics, Harvard University, Cambridge, MA 02138, USA*
[5] *Institute for Theoretical Physics, University of Innsbruck, A-6020 Innsbruck, Austria*
[6] *Center for Superconducting Physics and Materials, National Laboratory of Solid State Microstructures and Department of Physics, Nanjing University, Nanjing 210093, China*
[7] *Stanford PULSE Institute, SLAC National Accelerator Laboratory, Menlo Park, California 94025, USA*
[8] *Stanford Institute for Materials and Energy Sciences, SLAC National Accelerator Laboratory, Menlo Park, California 94025, USA*
[9] *Institute of Physics, Chinese Academy of Sciences, Beijing 100190, China*
[10] *Department of Physics and Astronomy, University of California, Los Angeles, CA 90095, USA*
[11] *Department of Physics, Tamkang University, Tamsui, New Taipei 25137, Taiwan*
[12] *Institute of Physics, Academia Sinica, Taipei 11529, Taiwan*
[13] *Laboratory for Topological Quantum Matter and Advanced Spectroscopy (B7), Department of Physics, Princeton University, Princeton, New Jersey 08544, USA*
[14] *Materials Sciences Division, Lawrence Berkeley National Laboratory, Berkeley, California 94720, USA*

I. INTRODUCTION

Symmetry plays a central role in conventional and topological phases of matter, making the ability to optically drive symmetry changes a critical step in developing future technologies that rely on such control. Topological materials, like the newly discovered topological semimetals, are particularly sensitive to a breaking or restoring of time-reversal and crystalline symmetries, which affect both bulk and surface electronic states. While previous studies have focused on controlling symmetry via coupling to the crystal lattice [1–5], we demonstrate here an all-electronic mechanism based on photocurrent generation. Using second-harmonic generation spectroscopy as a sensitive probe of symmetry changes [6, 7], we observe an ultrafast breaking of time-reversal and spatial symmetries following femtosecond optical excitation in the prototypical type-I Weyl semimetal TaAs. Our results show that optically driven photocurrents can be tailored to explicitly break electronic symmetry in a generic fashion, opening up the possibility of driving phase transitions between symmetry-protected states on ultrafast time scales.

Symmetry breaking has long defined the dominant paradigm for describing phase transitions in condensed matter systems. More recently, the discovery of novel topological phases, characterized by topological invariants as opposed to a local order parameter arising from spontaneously broken symmetry, provides an alternative framework for classifying states of matter [8, 9]. Nevertheless, symmetry continues to play a central role in the physics of topological materials, as it underlies topological protection in topological insulators and superconductors [10], crystalline topological phases [11], and the recently discovered topological semimetals [12–15]. In Dirac semimetals, symmetry protects the four-fold degeneracy of the Dirac point [16], while for Weyl semimetals (WSMs), the breaking of time-reversal or inversion symmetry allows for the crossing of two linearly dispersing, non-degenerate bands, giving rise to Weyl points [17–21]. These points act as monopoles of Berry curvature in momentum (k) space, and their presence leads to several unique experimental manifestations [19–26] that make these materials appealing for future technological applications [27].

Conventional probes of symmetry rely on diffractive techniques, like x-ray, neutron, and electron scattering, to determine the respective lattice, magnetic, and charge ordering in a crystal. Nonlinear optics is also an effective probe of symmetry, as the nonlinear response is described by a third (or higher) rank tensor [6, 7], allowing for phases hidden to linear probes (e.g., in correlated electron systems) to be revealed [28–31]. In the transition metal monopnictide (TMMP) family of WSMs, the lack of inversion symmetry resulting from a polar c-axis leads to an especially strong nonlinear optical response, with significant contributions from the generation of helicity-dependent injection [32–34] and helicity-independent shift [33, 35–38] photocurrents. Shift currents, resulting from a coherent shift of the electron cloud

* nsirica@lanl.gov
† rpprasan@lanl.gov

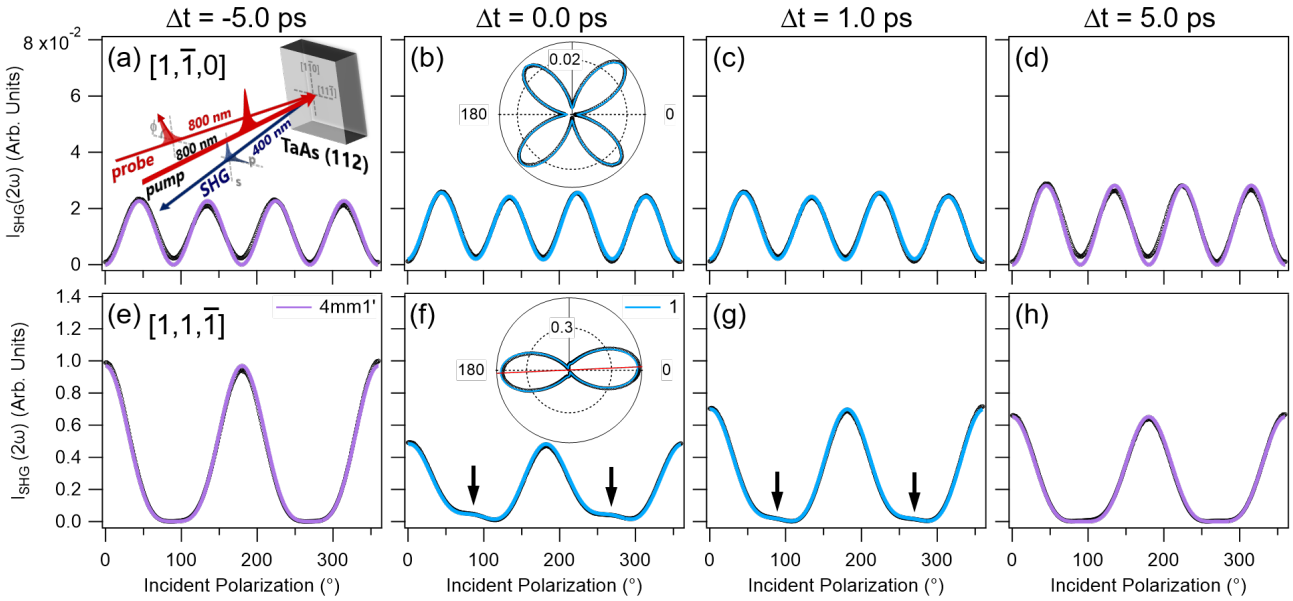

FIG. 1. Snapshots of the SHG pattern ($2\hbar\omega \sim 3.1$ eV) measured along the (a-d) [1,$\bar{1}$,0] and (e-h) [1,1,$\bar{1}$] axes for various pump delays: (a,e) $\Delta t = -5.0$ ps, (b,f) 0 ps, (c,g) 1.0 ps and (d,h) 5.0 ps. The inset in (a) shows a schematic of the experimental geometry, while insets in (b) and (f) show polar plots of the SHG pattern immediately following a linearly polarized pump excitation ($\hbar\omega$= 1.55 eV; fluence = 4.34 mJ/cm^2) aligned nearly along the [1,1,$\bar{1}$]) axis. Fits of the pattern assuming the magnetic point symmetries of $4mm1'$ ((a,e);(d,h)) and 1 ((b,f);(c,g)) are shown as solid purple and blue traces, respectively. Arrows in (f) and (g) denote the presence of transient, asymmetric lobes in the photoexcited state, while a small $\sim 2.5°$ rotation of the SHG pattern along [1,1,$\bar{1}$] is evident from the inset in (f).

in real space following photoexcitation [39], are particularly important, as they play a dominant role in both the giant, anisotropic second harmonic response [35, 36, 40] as well as the bulk photovoltaic effect [37] seen in WSMs, and may be traced to a difference in Berry connection between the bands participating in the optical transition [41, 42]. The most common nonlinear optical probe, second harmonic generation (SHG) spectroscopy, is thus sensitive to the asymmetric carrier distribution that accompanies photocurrent generation, making it a powerful tool for measuring the effect of transient photocurrents on material symmetry.

In this Letter, we show that femtosecond (fs) optical excitation transiently lowers the magnetic point symmetry $4mm1'$, with $1'$ indicating time-reversal symmetry, of the type-I WSM TaAs. Time-resolved SHG (TR-SHG) spectroscopy reveals this symmetry change occurs on a picosecond (ps) timescale, with no accompanying structural transition, indicating it to be purely electronic in origin. The strong nonlinear optical response exhibited by the TMMP WSMs [32–37, 41, 43–45] allows us to attribute this reduction in symmetry to changes in the spatial distribution of the electronic polarization that follow from photocurrent generation, supported by our previous terahertz (THz) emission experiments [33]. The degree of symmetry breaking is governed by the current direction, which we manipulate via the pump polarization. Our results demonstrate that optically driven photocurrents generically break electronic symmetries and can be used to achieve dynamic control of material properties on ultrafast time scales. This control mechanism will have wide ranging applications, particularly for topological semimetals, where symmetry is intimately tied to topology, opening up an original avenue of study rooted in current-induced symmetry breaking [46, 47].

II. RESULTS AND DISCUSSION

Prior to pump excitation, Figs. 1(a) and (e) show SHG patterns collected along the two in-plane [1,$\bar{1}$,0] and [1,1,$\bar{1}$] axes of the (112) face that are well described by a nonlinear susceptibility tensor, $\chi^{(2)}_{ijk}(2\omega)$, obeying the $4mm1'$ point group symmetry of TaAs (Section X of the supplementary information [48]). Here, the emitted second harmonic is dominated by an electric dipole response that is attributed to the polar c-axis. This is reflected by a large ratio of $\chi^{(2)}_{zzz}/\chi^{(2)}_{xxz} = 7.4$ at $\hbar\omega = 1.55$ eV (for z parallel to the crystallographic c-axis), as determined from our fits and in agreement with Refs. 35 and 36.

Following 1.55 eV photoexcitation, Figs. 1(f-h) show pronounced changes in the SHG pattern along [1,1,$\bar{1}$] that can be traced to a transient change in symmetry within the material when the pump polarization is nearly aligned along the [1,1,$\bar{1}$] axis. With the arrival of the pump pulse in Fig. 1(f), the emitted SHG along [1,1,$\bar{1}$] is reduced by half and the resultant pattern exhibits a 2.5°

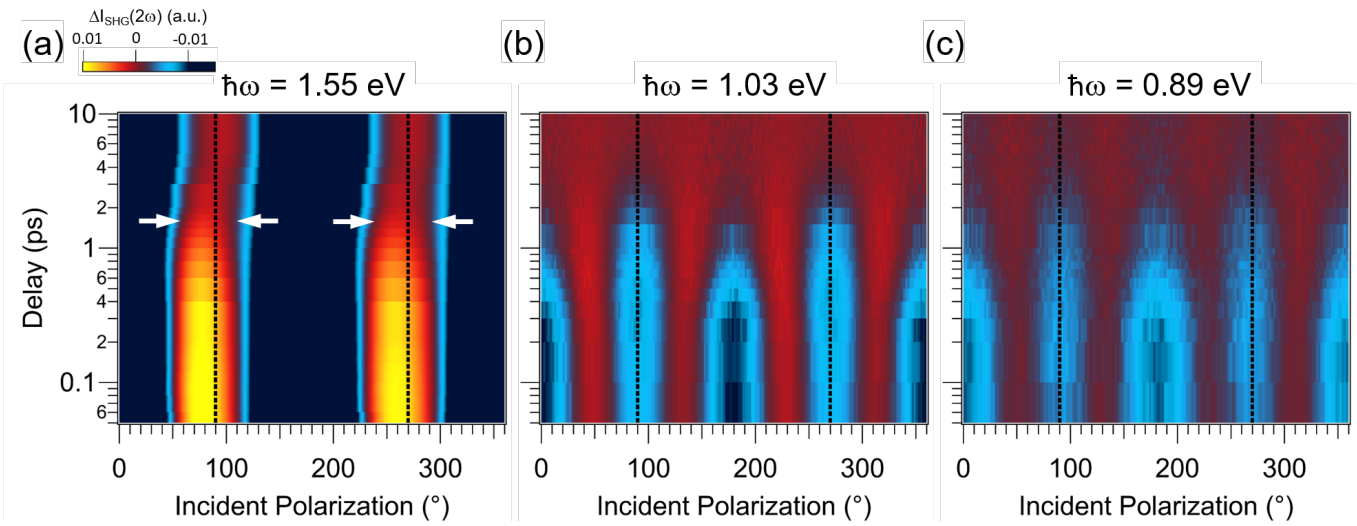

FIG. 2. Photoinduced polarization- and time-dependent changes in SHG intensity, $\Delta I_{\mathrm{SHG}}(2\omega)$, measured across the entire [1,1,$\bar{1}$] pattern after 1.55 eV photoexcitation (fluence = 4.34 mJ/cm^2) using probe energies of (a) $\hbar\omega = 1.55$ eV, (b) $\hbar\omega = 1.03$ eV, and (c) $\hbar\omega = 0.89$ eV (Fig. S1 [48]). Arrows in (a) denote the recovery of $4mm1'$ symmetry following the decay of the emergent, asymmetric lobes at $\sim 90^\circ$ and $\sim 270^\circ$ as well as a rotation of the SHG pattern back to equilibrium. Compared to panel (a), optical pumping at 1.55 eV does not change the symmetry of the patterns in panels (b-c), but suppresses them in a nearly isotropic manner over a $\Delta t < 2.0$ ps timescale (Fig. S2 [48]).

rotation with respect to equilibrium (inset of Fig. 1(f)). In addition, small lobes absent from the static pattern appear at $\sim 90^\circ$ and $\sim 270^\circ$ (Figs. 1(f-g)), whose asymmetry suggests a reduction of symmetry in the photoexcited state. In contrast, SHG patterns along [1,$\bar{1}$,0] grow in amplitude, with no additional rotation or spectral features appearing under pump excitation (Figs. 1(b-d)). From Fig. 1(g), both the rotation and asymmetric lobes in the [1,1,$\bar{1}$] TR-SHG pattern follow similar ultrafast dynamics, lasting $\tau_{PI} \sim 1.1$ ps before symmetry is restored and the intensity of the main lobes at 0° and 180° begins to recover back to its equilibrium value (Fig. 1(h)).

Coupling of the dynamics for both the rotation and lobe asymmetry in the TR-SHG spectra is further illustrated in Fig. 2, showing photoinduced polarization- and time-dependent changes over the entire [1,1,$\bar{1}$] pattern taken for the three probe energies used in our experiments. Fig. 2(a) reveals that both spectral features exhibit an equivalent time dependence, suggesting they originate from the same photoinduced symmetry-breaking transition, while Figs. 2(b-c) reveal an absence of symmetry breaking under non-resonant probe conditions (discussed further below). Together with separate time-resolved X-ray diffraction experiments (Fig. S3 [48, 49]), which show no structural dynamics over ultrafast timescales, but only on significantly longer timescales due to laser heating, this suggests an electronic origin of the symmetry breaking transition. Additionally, Fig. 2, along with symmetry considerations (Section X [48]), excludes the possibility that a dominant surface contribution, arising from a screened bulk response due to a high density of photoexcited carriers (10^{19} - 10^{20} cm^{-3}), is responsible for the reduced symmetry state, as such an effect would be evident at all probe energies. Hence, the mere generation of a photoexcited charge density is insufficient for lifting $4mm1'$ symmetry, and it is only when resonantly probing the transiently excited state that symmetry breaking in the SHG pattern is observed.

By reducing symmetry, the constraints imposed in equilibrium are lifted, necessitating that we consider a lower symmetry sub-group of $4mm1'$ to describe the time-dependent nonlinear susceptibility elements $\chi^{(2)}_{ijk}(2\omega;\Delta t)$, where ω and Δt denote frequency and time delay after pump excitation, respectively. To quantitatively extract information about the behavior of $\chi^{(2)}_{ijk}(2\omega;\Delta t)$, we simultaneously fit the SHG patterns collected along [1,$\bar{1}$,0] and [1,1,$\bar{1}$] as a function of pump delay and incident polarization angle, ϕ (Fig. 1). As compared to equilibrium, the rotation of the pattern along [1,1,$\bar{1}$] and the emergence of asymmetric lobes at 90° and 270° following photoexcitation cannot be accounted for under $4mm1'$ symmetry, as this requires the lobes to be both symmetric and pinned along the x and y axes. Rather, by considering the different subgroups of $4mm1'$, we find an optimal fit that captures the aforementioned features of the photoexcited state only in the absence of time-reversal and diagonal mirror, $m_{x,x,z}$, symmetry, described by the magnetic point group 1 (no point symmetries). Using the expression $I^{\alpha}_{\mathrm{SHG},\,1}(\phi) = \sum_{n=0}^{4} \mathcal{C}^{\alpha}_{n} \sin^{n}(\phi)\cos^{4-n}(\phi)$ ($\alpha = [1\bar{1}0], [11\bar{1}]$) for 1 symmetry over a $\Delta t < 2.0$ ps timescale allows us to associate different fit coefficients, $\mathcal{C}^{[11\bar{1}]}_{n}$, to specific features in the pattern (Section X [48]). The dynamics of these features are captured by the TR-SHG traces in

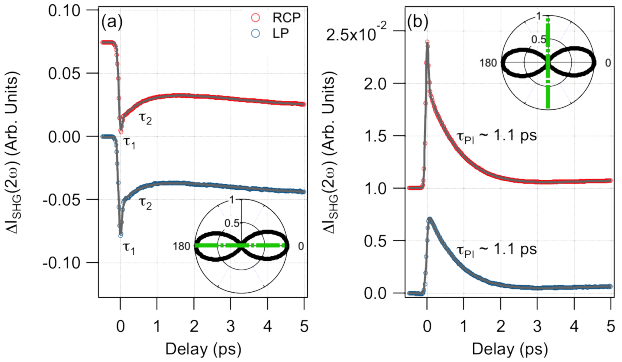

FIG. 3. Time-dependent traces of $\Delta I_{\mathrm{SHG}}(2\omega)$, measured for input probe polarizations along the green dashed lines of the [1,1,$\bar{1}$] SHG pattern shown as insets following 1.55 eV pump excitation. Here, (a) the suppression of the main lobe and (b) emergence of the photoinduced, asymmetric lobe are captured with high temporal resolution (< 100 fs). Fits of the dynamics following (blue) linearly and (red) circularly polarized pump excitation at a fluence of 4.34 mJ/cm^2 are superimposed onto the data, where traces generated under circularly polarized excitation have been offset for clarity. Traces in (a) show a pulsewidth-limited ultrafast component ($\tau_1 \sim 80$ fs) which is weakly dependent on pump polarization, while a similar ultrafast component develops only under helicity-dependent photoexcitation in (b) and arises from a sub-100 fs dichroic response (Fig. S4 [48]).

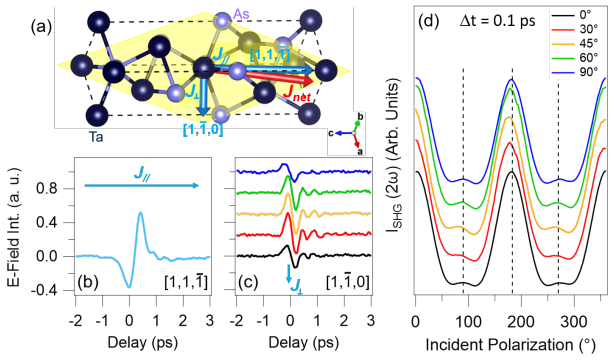

FIG. 4. (a) Schematic diagram of the net photocurrent contained within the (112) plane (yellow) of a TaAs unit cell. Emitted THz waveforms resulting from transient photocurrents generated along the (b) [1,1,$\bar{1}$] and (c) [1,$\bar{1}$,0] axes (offset for clarity) under linearly polarized pump excitation. (d) Changes in the transient SHG pattern ($\Delta t \sim 0.1$ ps) measured as a function of pump polarization relative to the [1,1,$\bar{1}$] axis (offset for clarity). The presence of an enhanced ($\sim 10\% - 20\%$), polarization-dependent shift current along [1,$\bar{1}$,0] leads to a clear reduction in symmetry within the pattern (Section IX [48]).

Fig. 3 ($\Delta I_{\mathrm{SHG}}(2\omega)$), plotted as a function of pump delay for select combinations of input and output probe polarizations. Fig. 3(a) captures the time dependence of the largest fit coefficient $\mathcal{C}_0^{[11\bar{1}]}$, depicting the suppression and subsequent recovery of the dominant lobe in the SHG pattern on a timescale defined by τ_1 and τ_2, while Fig. 3(b) shows the time dependence of $\mathcal{C}_4^{[11\bar{1}]}$, which illustrates the dynamics of the emergent, asymmetric lobe arising from photoexcitation.

Despite both $\mathcal{C}_0^{[11\bar{1}]}$ and $\mathcal{C}_4^{[11\bar{1}]}$ being allowed under $4mm1'$ symmetry (though $\mathcal{C}_4^{[11\bar{1}]}$ is small for the static pattern at $\hbar\omega = 1.55$ eV), a reduction to 1 symmetry is captured by the pair of odd fit parameters, $\mathcal{C}_1^{[11\bar{1}]}$ and $\mathcal{C}_3^{[11\bar{1}]}$, that quantitatively measure the degree of symmetry breaking imposed by the pump following photoexcitation (Section X [48]). These parameters result from breaking $m_{x,x,z}$ and enable fitting of the overall rotation in the pattern. However, as long as time-reversal symmetry remains, relations between the different $\mathcal{C}_n^{[11\bar{1}]}$ prevent these odd coefficients from capturing the observed asymmetry seen in our data. Rather, an accurate description requires a breaking of time-reversal symmetry to remove the constraints imposed on $\mathcal{C}_n^{[11\bar{1}]}$, revealing that both $m_{x,x,z}$ and time-reversal symmetry must be lifted in order to fully describe our experimental results. This reduction of symmetry from $4mm1'$ to 1 also allows for the emergence of additional fit parameters in the [1,$\bar{1}$,0] pattern, but these remain small and time-independent, consistent with the weaker ($\sim 100\times$) nonlinear response observed along this axis.

We emphasize that in contrast with the spontaneous symmetry breaking seen in conventional photoinduced phase transitions [50, 51], the symmetry breaking observed here is explicit and originates from the photoexcitation process itself. In this regard, the symmetry resolution gained from nonlinear optical probes like SHG provides a completely generic and robust framework for characterizing light-induced changes in the nonequilibrium state, as no underlying assumptions or reliance on theoretical models are required [6, 7]. While previous studies have reported explicit symmetry breaking from polarization-dependent photoexcitation in Bi and Sb that results from the coupling of phonons to a transiently excited charge density in k-space [52–54], we propose an alternative mechanism, which is entirely electronic in origin. Accounting for the fact that optical excitation creates a highly non-equilibrium state, we have carefully considered a number of possibilities, including a spatially inhomogeneous pump volume, anisotropic changes in optical constants, and carrier thermalization following photoexcitation, before concluding that the lowering of $4mm1'$ symmetry to 1 in TaAs most likely arises from photocurrent generation.

By having a well defined, but generic, direction relative to some high symmetry axis of the crystal, a photocurrent, $\vec{J}$, breaks both spatial and time-reversal symmetry through introducing an asymmetry in the nonequilibrium distribution of charge carriers along its direction that must necessarily be odd under time reversal. On the (112) face of TaAs, photocurrents originating from asymmetry in the real (shift) or k-space (injection)

carrier density are allowed to flow along the [1,1,$\bar{1}$] and [1,$\bar{1}$,0] axes [33, 34]. Here, a reduction in symmetry from $4mm1'$ to 1 occurs when a net current is directed away from either of these two high symmetry axes, breaking diagonal mirror symmetry (Fig. 4(a)) (Section X [48]). While a polarization-independent photocurrent is always present along [1,1,$\bar{1}$] (Fig. 4(b)) [33], the polarization dependence of the [1,$\bar{1}$,0] photocurrent allows us to break symmetry in a controllable manner by exploiting symmetry constraints placed on the shift current following linearly polarized excitation (Fig. 4(c)) (Section IX [48]). As shown in Fig. 4(d), varying the linear polarization of the excitation pulse relative to the [1,1,$\bar{1}$] axis causes the emergent photoinduced lobes in the transient SHG pattern ($\Delta t \sim 0.1$ ps) to develop a clear polarization-dependent asymmetry, while the pattern itself exhibits a rotation with respect to 0° and 180°. This is fully consistent with a reduction of symmetry brought on by an enhanced shift current response; as the pump polarization is detuned from the [1,1,$\bar{1}$] axis, shift currents along [1,$\bar{1}$,0] become symmetry allowed, with the largest contribution coming from an equal projection of the pump polarization along the two orthogonal axes of the (112) face (i.e. 45°) (Section IX [48]). This is reproduced by our data in Fig. 4(d), and illustrates our ability to exploit symmetry constraints on the photocurrent to tune the degree of symmetry breaking in this material. Similarly, after circularly polarized excitation, symmetry dictates that injection photocurrents can only flow along [1,$\bar{1}$,0], leading to an ultrafast reduction of $4mm1'$ to 1, as confirmed in Fig. 3(b) and Fig. S4 [48].

Ab initio calculations for the optical conductivity in TaAs reveal an As-p to Ta-d transition to be the major contribution to the in-plane conductivities, σ_{xx} and σ_{yy}, for our 1.55 eV excitation energy, while a Ta-d to Ta-d transition dominates the out-of-plane response, σ_{zz} (Section XII [48]). The fact that no symmetry changes are observed under non-degenerate pump excitation for either $\hbar\omega_{pump} > \hbar\omega_{probe}$ (Fig. 2(b-c)) or $\hbar\omega_{pump} < \hbar\omega_{probe}$ (Fig. S5 [48]) can thus be attributed to resonantly probing this initial photoexcited population of carriers. In other words, the transient asymmetry generated under 1.55 eV photoexcitation is lost over an ultrafast timescale due to momentum scattering, consistent with the bandwidth of the emitted THz pulses [33], and is therefore absent as photoexcited carriers relax to the lower lying, non-degenerate energy states probed at 0.89 eV - 1.03 eV (Fig. 2(b-c)). Further support is provided by band-resolved imaging of the photocurrent response in the topological insulator Bi_2Se_3, which reveals the transient asymmetry due to optically excited photocurrents is lost within ∼165 fs [55]. Hence, by using degenerate pump and probe energies, we ensured that only those states responsible for generating the photocurrent following pump excitation are probed; we note that any contribution arising from sum frequency generation can be discounted, since symmetry breaking in the TR-SHG pattern exists on timescales much longer than the temporal overlap of the pump and probe pulses.

Finally, our particular choice of photon energy was based on the giant anisotropic nonlinear response of the static SHG pattern along [1,1,$\bar{1}$] at 1.55 eV [35, 36]. While degenerate TR-SHG experiments performed at 1.02 eV show some dependence on pump polarization, similar to Fig. 4, the photoinduced change across the entire SHG pattern is dominated by a suppression of the SHG response, with the pattern itself retaining $4mm1'$ symmetry within our experimental resolution (Fig. S6 [48]). This is unsurprising, since the lack of spectral features at 90° and 270° in the static SHG pattern at 1.55 eV (Fig. 1(e)) as compared to lower photon energies (Fig. S1 (b-c)), makes this probe photon energy optimal for observing photocurrent-induced SHG along the orthogonal [1,$\bar{1}$,0] axis, as manifested by the emergent photoinduced lobes in Fig. 1(f-g).

In conclusion, by performing TR-SHG spectroscopy on the (112) surface of the WSM TaAs, we reveal a transient breaking of all magnetic point group symmetries following optical excitation, reducing the symmetry from $4mm1'$ to 1. Both the prompt recovery of equilibrium symmetry, as well as the absence of an ultrafast structural transition following optical excitation, suggest that light-induced symmetry breaking in TaAs originates from transient photocurrent generation. Specifically, the presence of a polar c-axis in the TMMP WSMs leads to a dominant helicity-independent, shift current whose geometric interpretation is rooted in an asymmetry in the electronic polarization introduced by optical excitation [36]. In this regard, our TR-SHG study reflects time-dependent changes to the polarization distribution that fail to respect both spatial and time-reversal symmetries, and whose relaxation is governed by a polarization-independent recovery, τ_{PI}, describing the return of the electronic polarization back to equilibrium.

The effect we report in this study originates from the fact that symmetry imposes general constraints on material properties, and thus can have important consequences for topological materials, where topology is closely related to symmetry. Since symmetry constrains the total number of Weyl nodes in TaAs, a reduction in symmetry brought on by photocurrent generation is expected to shift these nodes in both energy and momentum. This will alter the Fermi arc surface states, suggesting future time-and-angle-resolved photoemission spectroscopy experiments to directly measure the impact of transient photocurrents on the electronic band topology. More generally, our findings can be applied to any material system where either an optically generated or externally applied current breaks electronic symmetries. While generic, these results have important implications for topological semimetals [56], as the ability to alter symmetry on ultrafast timescales in these materials can lead to the potential realization of topological field effect transistors.

III. METHODS

A. Crystal Growth

TaAs single crystals were grown from polycrystalline samples by chemical vapor transport using iodine (2 mg/cm^3) as the transporting agent. Large polyhedral crystals with dimensions up to 1.5 mm were obtained in a temperature field of ΔT = 1150−1000°C following 3 weeks at growth temperature in an evacuated quartz ampoule. The as-grown three-dimensional (3D) crystals exhibit multiple surface facets, with the (112) face being identified by X-ray diffraction measurements.

B. Time-resolved SHG

TR-SHG experiments were performed on the (112) surface of different as-grown TaAs single crystals, sourced from entirely different batches, using an amplified Ti:Sapphire laser system operating at a 250 kHz repetition rate. SHG generated at near normal incidence (6°) from a linearly polarized optical probe tuned over a 0.89-1.55 eV (800 nm - 1400 nm) energy range was measured as a function of incident light polarization. A Glan-Taylor polarizer was used to select the emitted second harmonic polarized along the in-plane [1,$\bar{1}$,0] and [1,1,$\bar{1}$] high symmetry axes of the (112) face, as described in Ref. 57. Here, initial crystal alignment was performed by Laue diffraction, allowing us to hand scribe the direction of these two high symmetry axes (parallel to crystal face edge) on the sample mount (± 5°). Static and time-resolved SHG measurements were carried out in air or an optical cryostat, with the [1,1,$\bar{1}$] axis oriented parallel to the optical table. Initial pump and probe polarizations were aligned as closely to the [1,$\bar{1}$,0] and [1,1,$\bar{1}$] axes as possible, and verified through comparing the static SHG patterns measured here with those in literature [35, 36].

For excitation fluences ranging from 0.48 mJ/cm^2 - 6.03 mJ/cm^2 (Fig. S7 [48])), a normally incident, $\sim$ 80 fs optical pump pulse centered at 1.55 eV and either circularly or linearly polarized with respect to the [1,1,$\bar{1}$] axis creates a photocarrier density of 10^{19} - 10^{20} cm^{-3} within the 22 nm penetration depth [58]. In this pump fluence range, temperature (5-300 K) (Fig. S8 [48]) and pump polarization-dependent TR-SHG traces were measured for select combinations of input and output probe polarizations, while photoinduced changes across the entire SHG pattern were likewise collected at specific pump delays. In these experiments, a pump beam diameter 1.4× larger than the probe ensures that an initially homogeneous distribution of photoexcited carriers is measured. Finally, the generation of a photocurrent under pump excitation was ensured through working in the appropriate fluence range as well as observing THz-field induced second harmonic generation (TFISH) in the [1,$\bar{1}$,0] pattern, confirming the presence of a photocurrent under optical excitation [33].

C. Ab initio Calculations

First-principles calculations were performed using the OpenMX code, where norm-conserving pseudopotentials, optimized pseudoatomic basis functions, and the generalized gradient approximation were adopted [59–61]. Spin-orbit coupling was incorporated in these calculations through the use of j-dependent pseudopotentials [62]. For each Ta atom, three, two, two, and one optimized radial functions were allocated for the s, p, d, and f orbitals with a cutoff radius of 7 bohrs, respectively, denoted as Ta 7.0−s3p2d2f1. For each As atom, As 9.0−s3p3d3f2 was adopted. A cutoff energy of 1000 Ry was used for the numerical integration and for the solution of the Poisson equation. A $17 \times 17 \times 17$ k-point sampling in the first Brillouin zone was used, with experimental lattice parameters being adopted in these calculations. Such choice of parameters is consistent with those described elsewhere [63]. The density-of-states (DOS) was calculated using $80 \times 80 \times 80$ k-points, with a Gaussian broadening of 0.05 eV, for a primitive unit cell containing four atoms. The optical conductivity was then calculated via the Kubo-Greenwood formula using pseudoatomic basis functions [64]. Similarly, an $80 \times 80 \times 80$ k-point sampling, and a broadening parameter of $\eta = 0.05$ eV were adopted. For both of the ground-state and conductivity calculations, an electronic temperature of 300 K was used.

IV. AUTHOR CONTRIBUTIONS

TaAs single crystals were grown and characterized by L.X.Z., G.F.C., B.X., R.Y., B.S., N.N., and X.G.Q., with additional sample characterization and physical insights provided by T.A.C. and M.Z.H. N.S. and Y.M.D. performed the TR-SHG experiments with help from M.-C.L., P.P., and L.T.M. N.S., S.W.T., M.T., and R.P.P. performed the TR-XRD experiments with help from LCLS staff. The data was analyzed by N.S., P.P.O., and M.S.S. with a detailed symmetry analysis performed by P.P.O. and M.S.S. Ab initio calculations were carried out by C.-C.L. and H.L. with additional insight provided by J.-X.Z. The manuscript was written by N.S., P.P.O., M.S.S., and R.P.P. with significant contributions from S.A.T., A.J.T. and D.A.Y.

V. COMPETING INTERESTS

The authors declare no competing interests.

VI. DATA AVAILABILITY

All data presented in this manuscript can be made available upon reasonable request.

VII. ACKNOWLEDGEMENTS

This work was performed at the Center for Integrated Nanotechnologies at Los Alamos National Laboratory (LANL), a U.S. Department of Energy, Office of Basic Energy Sciences user facility, under user proposals #2017BC0064 and #2019AU0167. Use of the Linac Coherent Light Source (LCLS), SLAC National Accelerator Laboratory, is supported by the U.S. Department of Energy, Office of Science, Office of Basic Energy Sciences under Contract No. DE-AC02-76SF00515. N.S. and R.P.P. gratefully acknowledge the support of the U.S. Department of Energy through the LANL LDRD Program. P.P.O., J.-X.Z., and D.A.Y. are supported by the Center for Advancement of Topological Semimetals, an Energy Frontier Research Center funded by the U.S. Department of Energy Office of Science, Office of Basic Energy Sciences, through the Ames Laboratory under its Contract No. DE-AC02-07CH11358. T.A.C. and M.Z.H. acknowledge support from the U.S. Department of Energy under grant DE-FG-02-05ER46200. Work at UCLA was supported by the US DOE, Office of Science, Office of Basic Energy Sciences under award no. DE-SC0011978. M.S.S. acknowledges support from the National Science Foundation under Grant No. DMR-1664842. C.-C.L. acknowledges the Ministry of Science and Technology of Taiwan for financial support under contract No. MOST 108-2112-M-032-010-MY2. T.A.C. was supported by the National Science Foundation Graduate Research Fellowship Program under Grant No. DGE-1656466. M.T., and S.W.T. were supported by the U.S. Department of Energy, Office of Science, Office of Basic Energy Sciences through the Division of Materials Sciences and Engineering under Contract No. DE-AC02-76SF00515. We thank Yu-Miin Sheu for the helpful discussion.

[1] E. J. Sie, C. M. Nyby, C. D. Pemmaraju, S. J. Park, X. Shen, J. Yang, M. C. Hoffmann, B. K. Ofori-Okai, R. Li, A. H. Reid, S. Weathersby, E. Mannebach, N. Finney, D. Rhodes, D. Chenet, A. Antony, L. Balicas, J. Hone, T. P. Devereaux, T. F. Heinz, X. Wang, and A. M. Lindenberg, An ultrafast symmetry switch in a Weyl semimetal, Nature **565**, 61 (2019).

[2] J. L. Collins, A. Tadich, W. Wu, L. C. Gomes, J. N. B. Rodrigues, C. Liu, J. Hellerstedt, H. Ryu, S. Tang, S.-K. Mo, S. Adam, S. A. Yang, M. S. Fuhrer, and M. T. Edmonds, Electric-field-tuned topological phase transition in ultrathin Na_3Bi, Nature **564**, 390 (2018).

[3] J. Mutch, W.-C. Chen, P. Went, T. Qian, I. Z. Wilson, A. Andreev, C.-C. Chen, and J.-H. Chu, Evidence for a strain-tuned topological phase transition in $ZrTe_5$, Science Advances **5**, eaav9771 (2019).

[4] C. Vaswani, L.-L. Wang, D. H. Mudiyanselage, Q. Li, P. M. Lozano, G. D. Gu, D. Cheng, B. Song, L. Luo, R. H. J. Kim, C. Huang, Z. Liu, M. Mootz, I. E. Perakis, Y. Yao, K. M. Ho, and J. Wang, Light-driven raman coherence as a nonthermal route to ultrafast topology switching in a dirac semimetal, Phys. Rev. X **10**, 021013 (2020).

[5] L. Luo, D. Cheng, B. Song, L.-L. Wang, C. Vaswani, P. M. Lozano, G. Gu, C. Huang, R. H. J. Kim, Z. Liu, J.-M. Park, Y. Yao, K. Ho, I. E. Perakis, Q. Li, and J. Wang, A light-induced phononic symmetry switch and giant dissipationless topological photocurrent in $ZrTe_5$, Nature Materials **20**, 329 (2021).

[6] D. H. Torchinsky and D. Hsieh, Rotational Anisotropy Nonlinear Harmonic Generation, in *Magnetic Characterization Techniques for Nanomaterials*, edited by C. S. Kumar (Springer Berlin Heidelberg, Berlin, Heidelberg, 2017) pp. 1–49.

[7] L. Zhao, D. Torchinsky, J. Harter, A. de la Torre, and D. Hsieh, Second Harmonic Generation Spectroscopy of Hidden Phases, in *Encyclopedia of Modern Optics (Second Edition)*, edited by B. D. Guenther and D. G. Steel (Elsevier, Oxford, 2018) second edition ed., pp. 207 – 226.

[8] X.-G. Wen, Topological orders and edge excitations in fractional quantum Hall states, Advances in Physics **44**, 405 (1995).

[9] S. Sachdev, Topological order, emergent gauge fields, and Fermi surface reconstruction, Reports on Progress in Physics **82**, 014001 (2019), arXiv:1801.01125 [cond-mat.str-el].

[10] M. Z. Hasan and C. L. Kane, Colloquium: Topological insulators, Rev. Mod. Phys. **82**, 3045 (2010).

[11] Y. Ando and L. Fu, Topological Crystalline Insulators and Topological Superconductors: From Concepts to Materials, Annual Review of Condensed Matter Physics **6**, 361 (2015).

[12] H. Gao, J. W. Venderbos, Y. Kim, and A. M. Rappe, Topological Semimetals from First Principles, Annual Review of Materials Research **49**, 153 (2019).

[13] N. P. Armitage, E. J. Mele, and A. Vishwanath, Weyl and Dirac semimetals in three-dimensional solids, Rev. Mod. Phys. **90**, 015001 (2018).

[14] M. Hasan, S.-Y. Xu, I. Belopolski, and S. H. Huang, Discovery of Weyl Fermion Semimetals and Topological Fermi Arc States, Annu. Rev. Condens. Matter Phys. **8**, 289 (2017).

[15] B. Yan and C. Felser, Topological Materials: Weyl Semimetals, Annual Review of Condensed Matter Physics **8**, 337 (2017).

[16] S. M. Young, S. Zaheer, J. C. Y. Teo, C. L. Kane, E. J. Mele, and A. M. Rappe, Dirac Semimetal in Three Dimensions, Phys. Rev. Lett. **108**, 140405 (2012).

[17] X. Wan, A. M. Turner, A. Vishwanath, and S. Y. Savrasov, Topological semimetal and Fermi-arc surface states in the electronic structure of pyrochlore iridates, Phys. Rev. B **83**, 205101 (2011).

[18] G. Xu, H. Weng, Z. Wang, X. Dai, and Z. Fang, Chern Semimetal and the Quantized Anomalous Hall Effect in $HgCr_2Se_4$, Phys. Rev. Lett. **107**, 186806 (2011).

[19] S.-Y. Xu, I. Belopolski, N. Alidoust, M. Neupane, G. Bian, C. Zhang, R. Sankar, G. Chang, Z. Yuan, C.-C. Lee, S.-M. Huang, H. Zheng, J. Ma, D. S. Sanchez, B. Wang, A. Bansil, F. Chou, P. P. Shibayev, H. Lin,

S. Jia, and M. Z. Hasan, Discovery of a Weyl fermion semimetal and topological Fermi arcs, Science **349**, 613 (2015).

[20] B. Q. Lv, N. Xu, H. M. Weng, J. Z. Ma, P. Richard, X. C. Huang, L. X. Zhao, G. F. Chen, C. E. Matt, F. Bisti, V. N. Strocov, J. Mesot, Z. Fang, X. Dai, T. Qian, M. Shi, and H. Ding, Observation of Weyl nodes in TaAs, Nature Physics **11**, 724 (2015).

[21] L. X. Yang, Z. K. Liu, Y. Sun, H. Peng, H. F. Yang, T. Zhang, B. Zhou, Y. Zhang, Y. F. Guo, M. Rahn, D. Prabhakaran, Z. Hussain, S.-K. Mo, C. Felser, B. Yan, and Y. L. Chen, Weyl semimetal phase in the noncentrosymmetric compound TaAs, Nature Physics **11**, 728 (2015).

[22] Z. K. Liu, L. X. Yang, Y. Sun, T. Zhang, H. Peng, H. F. Yang, C. Chen, Y. Zhang, Y. Guo, D. Prabhakaran, M. Schmidt, Z. Hussain, S.-K. Mo, C. Felser, B. Yan, and Y. L. Chen, Evolution of the Fermi surface of Weyl semimetals in the transition metal pnictide family, Nature Materials **15**, 27 (2015).

[23] S. Jia, S.-Y. Xu, and M. Z. Hasan, Weyl semimetals, Fermi arcs and chiral anomalies, Nature Materials **15**, 1140 (2016).

[24] S. A. Parameswaran, T. Grover, D. A. Abanin, D. A. Pesin, and A. Vishwanath, Probing the Chiral Anomaly with Nonlocal Transport in Three-Dimensional Topological Semimetals, Phys. Rev. X **4**, 031035 (2014).

[25] X. Huang, L. Zhao, Y. Long, P. Wang, D. Chen, Z. Yang, H. Liang, M. Xue, H. Weng, Z. Fang, X. Dai, and G. Chen, Observation of the Chiral-Anomaly-Induced Negative Magnetoresistance in 3D Weyl Semimetal TaAs, Phys. Rev. X **5**, 031023 (2015).

[26] C.-L. Zhang, S.-Y. Xu, I. Belopolski, Z. Yuan, Z. Lin, B. Tong, G. Bian, N. Alidoust, C.-C. Lee, S.-M. Huang, T.-R. Chang, G. Chang, C.-H. Hsu, H.-T. Jeng, M. Neupane, D. S. Sanchez, H. Zheng, J. Wang, H. Lin, C. Zhang, H.-Z. Lu, S.-Q. Shen, T. Neupert, M. Zahid Hasan, and S. Jia, Signatures of the Adler - Bell - Jackiw chiral anomaly in a Weyl fermion semimetal, Nature Communications **7**, 10735 (2016).

[27] Y. Tokura, M. Kawasaki, and N. Nagaosa, Emergent functions of quantum materials, Nature Physics **13**, 1056 (2017).

[28] L. Zhao, D. H. Torchinsky, H. Chu, V. Ivanov, R. Lifshitz, R. Flint, T. Qi, G. Cao, and D. Hsieh, Evidence of an odd-parity hidden order in a spinorbit coupled correlated iridate, Nature Physics **12**, 32 (2016).

[29] J. W. Harter, Z. Y. Zhao, J.-Q. Yan, D. G. Mandrus, and D. Hsieh, A parity-breaking electronic nematic phase transition in the spin-orbit coupled metal $Cd_2Re_2O_7$, Science **356**, 295 (2017).

[30] B. B. Van Aken, J.-P. Rivera, H. Schmid, and M. Fiebig, Observation of ferrotoroidic domains, Nature **449**, 702 (2007).

[31] W. Jin, E. Drueke, S. Li, A. Admasu, R. Owen, M. Day, K. Sun, S.-W. Cheong, and L. Zhao, Observation of a ferro-rotational order coupled with second-order nonlinear optical fields, Nature Physics **16**, 42 (2020).

[32] Q. Ma, S.-Y. Xu, C.-K. Chan, C.-L. Zhang, G. Chang, Y. Lin, W. Xie, T. Palacios, H. Lin, S. Jia, P. A. Lee, P. Jarillo-Herrero, and N. Gedik, Direct optical detection of Weyl fermion chirality in a topological semimetal, Nature Physics **13**, 842 (2017).

[33] N. Sirica, R. I. Tobey, L. X. Zhao, G. F. Chen, B. Xu, R. Yang, B. Shen, D. A. Yarotski, P. Bowlan, S. A. Trugman, J.-X. Zhu, Y. M. Dai, A. K. Azad, N. Ni, X. G. Qiu, A. J. Taylor, and R. P. Prasankumar, Tracking Ultrafast Photocurrents in the Weyl Semimetal TaAs Using THz Emission Spectroscopy, Phys. Rev. Lett. **122**, 197401 (2019).

[34] Y. Gao, S. Kaushik, E. J. Philip, Z. Li, Y. Qin, W. L. Liu, Y. P. andZhang, Y. L. Su, X. Chen, H. Weng, D. E. Kharzeev, M. K. Liu, and J. Qi, Chiral terahertz wave emission from the Weyl semimetal TaAs, Nature Communications **11**, 720 (2020).

[35] L. Wu, S. Patankar, T. Morimoto, N. L. Nair, E. Thewalt, A. Little, J. G. Analytis, J. E. Moore, and J. Orenstein, Giant anisotropic nonlinear optical response in transition metal monopnictide Weyl semimetals, Nature Physics **13**, 350 (2016).

[36] S. Patankar, L. Wu, B. Lu, M. Rai, J. D. Tran, T. Morimoto, D. E. Parker, A. G. Grushin, N. L. Nair, J. G. Analytis, J. E. Moore, J. Orenstein, and D. H. Torchinsky, Resonance-enhanced optical nonlinearity in the Weyl semimetal TaAs, Phys. Rev. B **98**, 165113 (2018).

[37] G. B. Osterhoudt, L. K. Diebel, X. Yang, J. Stanco, X. Huang, B. Shen, N. Ni, P. Moll, Y. Ran, and K. S. Burch, Colossal Photovoltaic Effect Driven by the Singular Berry Curvature in a Weyl Semimetal, Nature Materials **18**, 471 (2019).

[38] J. Ma, Q. Gu, Y. Liu, J. Lai, P. Yu, X. Zhuo, Z. Liu, J.-H. Chen, J. Feng, and D. Sun, Nonlinear photoresponse of type-ii weyl semimetals, Nature Materials **18**, 476 (2019).

[39] J. E. Sipe and A. I. Shkrebtii, Second-order optical response in semiconductors, Phys. Rev. B **61**, 5337 (2000).

[40] Z. Li, Y.-Q. Jin, T. Tohyama, T. Iitaka, J.-X. Zhang, and H. Su, Second harmonic generation in the Weyl semimetal TaAs from a quantum kinetic equation, Phys. Rev. B **97**, 085201 (2018).

[41] T. Morimoto and N. Nagaosa, Topological nature of nonlinear optical effects in solids, Science Advances **2**, 1501524 (2016).

[42] M. Sotome, M. Nakamura, J. Fujioka, M. Ogino, Y. Kaneko, T. Morimoto, Y. Zhang, M. Kawasaki, N. Nagaosa, Y. Tokura, and N. Ogawa, Spectral dynamics of shift current in ferroelectric semiconductor SbSI, Proceedings of the National Academy of Sciences **116**, 1929 (2019), https://www.pnas.org/content/116/6/1929.full.pdf.

[43] D. E. Parker, T. Morimoto, J. Orenstein, and J. E. Moore, Diagrammatic approach to nonlinear optical response with application to Weyl semimetals, Phys. Rev. B **99**, 045121 (2019).

[44] C. P. Weber, B. S. Berggren, M. G. Masten, T. C. Ogloza, S. Deckoff-Jones, J. Mado, M. K. L. Man, K. M. Dani, L. Zhao, G. Chen, J. Liu, Z. Mao, L. M. Schoop, B. V. Lotsch, S. S. P. Parkin, and M. Ali, Similar ultrafast dynamics of several dissimilar Dirac and Weyl semimetals, Journal of Applied Physics **122**, 223102 (2017).

[45] C. P. Weber, Ultrafast investigation and control of Dirac and Weyl semimetals, Journal of Applied Physics **129**, 070901 (2021), https://doi.org/10.1063/5.0035878.

[46] J. B. Khurgin, Current induced second harmonic generation in semiconductors, Applied Physics Letters **67**, 1113 (1995), https://doi.org/10.1063/1.114978.

[47] B. A. Ruzicka, L. K. Werake, G. Xu, J. B. Khurgin, E. Y. Sherman, J. Z. Wu, and H. Zhao, Second-Harmonic Gen-

eration Induced by Electric Currents in GaAs, Phys. Rev. Lett. **108**, 077403 (2012).

[48] See supplementary information for a more detailed discussion of supporting figures and derivations.

[49] M.-C. Lee, N. Sirica, S. W. Teitelbaum, A. Maznev, T. Pezeril, R. Tutchton, V. Krapivin, G. A. de la Pena, Y. Huang, L. X. Zhao, G. F. Chen, B. Xu, R. Yang, J. Shi, J. X. Zhu, D. A. Yarotski, X. G. Qiu, K. A. Nelson, M. Trigo, D. A. Reis, and R. P. Prasankumar, Direct Observation of Coherent Longitudinal and Shear Acoustic Phonons in the Weyl Semimetal TaAs Using Ultrafast X-ray Diffraction, arXiv:2011.07196 (2020).

[50] A. Zong, A. Kogar, Y.-Q. Bie, T. Rohwer, C. Lee, E. Baldini, E. Ergeen, M. B. Yilmaz, B. Freelon, E. J. Sie, H. Zhou, J. Straquadine, P. Walmsley, P. E. Dolgirev, A. V. Rozhkov, I. R. Fisher, P. Jarillo-Herrero, B. V. Fine, and N. Gedik, Evidence for topological defects in a photoinduced phase transition, Nature Physics **15**, 27 (2019).

[51] A. Zong, P. E. Dolgirev, A. Kogar, E. Erge, M. B. Yilmaz, Y.-Q. Bie, T. Rohwer, I.-C. Tung, J. Straquadine, X. Wang, Y. Yang, X. Shen, R. Li, J. Yang, S. Park, M. C. Hoffmann, B. K. Ofori-Okai, M. E. Kozina, H. Wen, X. Wang, I. R. Fisher, P. Jarillo-Herrero, and N. Gedik, Dynamical Slowing-Down in an Ultrafast Photoinduced Phase Transition, Phys. Rev. Lett. **123**, 097601 (2019).

[52] J. J. Li, J. Chen, D. A. Reis, S. Fahy, and R. Merlin, Optical Probing of Ultrafast Electronic Decay in Bi and Sb with Slow Phonons, Phys. Rev. Lett. **110**, 047401 (2013).

[53] E. D. Murray and S. Fahy, First-Principles Calculation of Femtosecond Symmetry-Breaking Atomic Forces in Photoexcited Bismuth, Phys. Rev. Lett. **114**, 055502 (2015).

[54] S. M. O'Mahony, F. Murphy-Armando, E. D. Murray, J. D. Querales-Flores, I. Savić, and S. Fahy, Ultrafast Relaxation of Symmetry-Breaking Photo-Induced Atomic Forces, Phys. Rev. Lett. **123**, 087401 (2019).

[55] H. Soifer, A. Gauthier, A. F. Kemper, C. R. Rotundu, S.-L. Yang, H. Xiong, D. Lu, M. Hashimoto, P. S. Kirchmann, J. A. Sobota, and Z.-X. Shen, Band-Resolved Imaging of Photocurrent in a Topological Insulator, Phys. Rev. Lett. **122**, 167401 (2019).

[56] K. Takasan, T. Morimoto, J. Orenstein, and J. E. Moore, Current-induced second harmonic generation in inversion-symmetric Dirac and Weyl semimetals, arXiv:2007.08887 (2020).

[57] Y. M. Sheu, S. A. Trugman, L. Yan, Q. X. Jia, A. J. Taylor, and R. P. Prasankumar, Using ultrashort optical pulses to couple ferroelectric and ferromagnetic order in an oxide heterostructure, Nature Communications **5**, 5832 (2014).

[58] B. Xu, Y. M. Dai, L. X. Zhao, K. Wang, R. Yang, W. Zhang, J. Y. Liu, H. Xiao, G. F. Chen, A. J. Taylor, D. A. Yarotski, R. P. Prasankumar, and X. G. Qiu, Optical spectroscopy of the Weyl semimetal TaAs, Phys. Rev. B **93**, 121110 (2016).

[59] T. Ozaki, Variationally optimized atomic orbitals for large-scale electronic structures, Phys. Rev. B **67**, 155108 (2003).

[60] I. Morrison, D. M. Bylander, and L. Kleinman, Nonlocal Hermitian norm-conserving Vanderbilt pseudopotential, Phys. Rev. B **47**, 6728 (1993).

[61] J. P. Perdew, K. Burke, and M. Ernzerhof, Generalized Gradient Approximation Made Simple, Phys. Rev. Lett. **77**, 3865 (1996).

[62] G. Theurich and N. A. Hill, Self-consistent treatment of spin-orbit coupling in solids using relativistic fully separable ab initio pseudopotentials, Phys. Rev. B **64**, 073106 (2001).

[63] C.-C. Lee, S.-Y. Xu, S.-M. Huang, D. S. Sanchez, I. Belopolski, G. Chang, G. Bian, N. Alidoust, H. Zheng, M. Neupane, B. Wang, A. Bansil, M. Z. Hasan, and H. Lin, Fermi surface interconnectivity and topology in Weyl fermion semimetals TaAs, TaP, NbAs, and NbP, Phys. Rev. B **92**, 235104 (2015).

[64] C.-C. Lee, Y.-T. Lee, M. Fukuda, and T. Ozaki, Tight-binding calculations of optical matrix elements for conductivity using nonorthogonal atomic orbitals: Anomalous Hall conductivity in bcc Fe, Phys. Rev. B **98**, 115115 (2018).